

Version as of January 5, 2018

Dominance of Nuclear Processes in the Dissociation of ${}^8\text{B}$

C.H. Dasso ^a, S.M. Lenzi ^b and A. Vitturi ^b

ECT*, Strada delle Tabarelle 286, I-38050 Trento, Italy
and The Niels Bohr Institute, Blegdamsvej 17, Copenhagen Ø, Denmark ^a

Dipartimento di Fisica and INFN, Università di Padova, Padova, Italy ^b

Abstract:

We study the break-up of ${}^8\text{B}$ in collisions with heavy-ions. The process is described in terms of inelastic excitations leading to states in the continuum. The effects of the nuclear and Coulomb fields induced by the reaction partner are included on the same footing in the microscopic construction of the transition matrix elements. At variance with previous findings, the contribution of the nuclear component is found to be comparable to – and even larger than – that of the Coulomb one. Because of the weak binding energy of ${}^8\text{B}$ the nuclear couplings associated with inelastic excitation to low-lying states in the continuum extend to unusually large distances. As a consequence, the interplay between nuclear and Coulomb excitation processes differs significantly from the situation encountered in reactions involving systems close to the stability line. In particular, nuclear excitation is found to remain predominant at energies well below the Coulomb barrier.

PACS numbers: 21.60.-n, 23.20.Js

1. Introduction

One of the most interesting aspects of nuclear systems at the nucleon drip-lines is the prediction (supported by experimental evidence) of strong concentrations of strength in the multipole response at excitation energies near the continuum threshold for particle emission. It has been shown in a series of investigations¹⁻³⁾ that this strength is not associated with the existence of a low-lying collective mode but, rather, a characteristic feature of the single-particle response for weakly-bound systems. This arises from the possibility of setting up a favorable matching between the long range of the bound orbitals and the wavelength of scattering states in the continuum. Although it is not readily appreciated, this argument invokes the single-particle transition density and it is not thus restricted to electromagnetic processes.

Conventional wisdom takes for granted that Coulomb excitation has a long interaction range while nuclear processes only become important at relative distances comparable to the sum of the nuclear radii. This is why even today, in the investigation of break-up processes of weakly-bound systems close to the drip-line, attention is focused in the role of the former and nuclear effects have been often ignored.

A radically different picture emerges, however, when one considers the most general origin of nuclear transition couplings and forsakes concepts specifically tied to ordinary collective modes. If the presence of loosely-bound orbitals pushes out the inelastic transition densities into the continuum to radial ranges in the order of 15–25 fm, consequences of this significant shift will *inevitably reflect in both the Coulomb and nuclear formfactors*. Thus one can anticipate situations for weakly-bound neutron/proton-rich systems where the nuclear couplings may still be dominant under the diluted-density conditions that prevail at separation distances of the order of 20 fm.

The possibility of observing such effects is tantalizing and we intend in this contribution to provide concrete estimates for the radial ranges that are likely to

be relevant in actual measurements. To this end we consider in what follows the break-up of ${}^8\text{B}$ into ${}^7\text{Be}$ induced by a high-energy collision with lead nuclei, a case experimentally explored in ref. ⁴⁾. Furthermore, to illustrate how critical it can be the extension of ordinary “safe-distance” concepts into reactions involving weakly-bound systems we shall also examine the same break-up process but on low-energy collisions with a nickel target, a reaction discussed in ref. ⁵⁾.

In Section 2 we introduce the expressions used to construct the matrix elements that induce single-particle proton transitions into the continuum. A brief review of a coupled-channel formalism to evaluate semiclassical reaction amplitudes is also included here. Results of this calculation scheme in terms of transition densities, formfactors, cross sections and Q-value distributions are given in Section 3. More specifically, Section 4 is devoted to reactions at energies below the barrier. Examples of angular distributions are shown in this context. Concluding remarks close the presentation in Section 5.

2. Formalism

Microscopic calculations of formfactors for inelastic transitions have been routinely performed in the past. See, for example the review article in ref. ⁶⁾. The basic expressions that are found in the literature need only be adapted to account for the coupling scheme that is exploited in our specific application. We adhere here to the familiar prescription ⁷⁾ in which the ground state of ${}^8\text{B}$ is obtained by coupling the valence proton in a single-particle $p_{3/2}$ state with an inert ${}^7\text{Be}$ core with quantum numbers $I_c^\pi=3/2^-$. The experimentally known binding energy (-0.14 MeV) can then be reproduced by choosing a single particle potential for the protons with a Woods-Saxon shape and parameters $V_o=-44.66$ MeV, $r_o=1.25$ fm, $a_o=0.52$ fm and a spin-orbit coupling of $F_{so}=0.351$ MeV. Excited configurations of ${}^8\text{B}$ follow from the same coupling scheme but include a suitable adjustment of the depth of the single-particle potential, V_o , to reproduce the corresponding binding energies. For a table of potential parameters covering these situations cf. ref. ⁷⁾.

We start by writing the projectile wavefunction for the initial state with angular momentum quantum numbers J_i, M_i as

$$\Psi_{J_i M_i} = \sum_{m_1 m_c} \langle j_1 m_1 j_c m_c | J_i M_i \rangle \psi_{n_1 \ell_1 j_1 m_1}(\vec{r}, \sigma) \phi_{c, j_c m_c}(\vec{r}_c, \sigma_c), \quad (1)$$

where \vec{r} , σ are the space and spin variables for the proton and \vec{r}_c , σ_c are the corresponding global quantities for the ${}^7\text{Be}$ core. The single-particle proton wavefunction ψ corresponds to a bound state and is fully determined by specifying, in addition to j_1 , m_1 , the principal quantum number n_1 and the orbital angular momentum ℓ_1 . Similarly, for the final state we use

$$\Psi_{J_f M_f} = \sum_{m_2 m'_c} \langle j_2 m_2 j_c m'_c | J_f M_f \rangle \psi_{E \ell_2 j_2 m_2}(\vec{r}, \sigma) \phi_{c, j_c m'_c}(\vec{r}_c, \sigma_c), \quad (2)$$

where the fundamental difference with (1) is that the single-particle proton function corresponds now to a scattering state in the continuum and is thus labeled by the energy E . Only the modulus of \vec{k} enters in the identification of the states, its orientations being incorporated in a proper normalization factor⁸⁾.

The matrix elements of the one-body excitation operator $V(|\vec{r} - \vec{R}|)$ – involving only the proton coordinates and the distance \vec{R} between the reactants – introduce a straightforward integration over \vec{r}_c , σ_c . This yields a $\delta_{m_c m'_c}$ which, in turn, sets $m_1 = M_i - m_c$ and $m_2 = M_f - m_c$. Thus, the formfactor for the inelastic transition of the proton into the continuum can be written as

$$F_{J_i M_i \rightarrow J_f M_f}(\vec{R}) = \sum_{m_c} \langle j_1(M_i - m_c) j_c m_c | J_i M_i \rangle \langle j_2(M_f - m_c) j_c m_c | J_f M_f \rangle f_{n_1 \ell_1 j_1(M_i - m_c) \rightarrow E \ell_2 j_2(M_f - m_c)}(\vec{R}). \quad (3)$$

Here the function f stands for the basic building block in the microscopic construction of inelastic formfactors, namely the matrix element inducing the transition of the valence proton between two pure single-particle states,

$$f_{n_1 \ell_1 j_1(M_i - m_c) \rightarrow E \ell_2 j_2(M_f - m_c)}(\vec{R}) =$$

$$\begin{aligned}
 &= \sqrt{\pi} \sum_{\lambda} (-1)^{M_f - m_c + \frac{1}{2}} \delta(\ell_1 + \ell_2 + \lambda, \text{even}) \langle j_1 \frac{1}{2} j_2 - \frac{1}{2} | \lambda 0 \rangle \\
 &\times \frac{\sqrt{2j_1 + 1} \sqrt{2j_2 + 1}}{\sqrt{2\lambda + 1}} \langle j_1(m_c - M_i) j_2(M_f - m_c) | L(M_f - M_i) \rangle Y_{\lambda(M_i - M_f)}(\hat{R}) \\
 &\times \left[\int_0^{\infty} r^2 dr \int_{-1}^{+1} du R_{E\ell_2 j_2}^*(r) R_{n_1 \ell_1 j_1}(r) V(\sqrt{r^2 + R^2 - 2rRu}) P_{\lambda}(u) \right] . \quad (4)
 \end{aligned}$$

We distinguish at this point the nuclear and Coulomb components of the excitation field, $V = V^N + V^C$. The former involves the mean field felt by the proton due to the presence of the target and is generally parameterized by a Woods-Saxon function of the form

$$V^N(|\vec{r} - \vec{R}|) = \frac{V_{pT}}{1 + \exp [(|\vec{r} - \vec{R}| - R_T) / a_{pT}]} . \quad (5)$$

The quantities V_{pT} and a_{pT} should not be confused with the potential depth and diffuseness previously invoked (that referred to the projectile mean field). They assume, nevertheless, close numerical values¹³⁾. The Coulomb component is given by

$$V^C(|\vec{r} - \vec{R}|) = \Phi_0 \frac{R_T}{|\vec{r} - \vec{R}|} , \quad \text{for } |\vec{r} - \vec{R}| \geq R_T \quad (6)$$

$$V^C(|\vec{r} - \vec{R}|) = \Phi_0 \left[\frac{3}{2} - \frac{|\vec{r} - \vec{R}|^2}{2R_T^2} \right] , \quad \text{for } |\vec{r} - \vec{R}| < R_T \quad (7)$$

in terms of $\Phi_0 = z_{ef} z_T e^2 / R_T$. The effective charge is equal to one for all multipolarities except $\lambda=1$, when $z_{ef} = N_P / A_P$ ensures that no spurious motion of the center of mass takes place.

The screening effects taken into account by the splitting of the Coulomb field into the two expressions (6,7) are often ignored. Conceptually more disturbing is, however, the fact that standard analyses of the Coulomb excitation processes for neutron-rich, weakly-bound systems have consistently relied on the effects of the multipole response to the field r^λ . This came about from a rather uncritical use of the expression

$$\frac{1}{\sqrt{r^2 + R^2 - 2rRu}} = \sum_L \frac{r^\lambda}{R^{\lambda+1}} P_\lambda(u) . \quad (8)$$

which allows – when introduced in (4) – to perform the integral over u analytically and thus reduce the radial dependence of the Coulomb formfactors to the familiar $R^{-\lambda-1}$ form. The expansion (8) is, however, valid only when $r < R$. This may be a reasonable assumption for Coulomb excitation in reactions with stable systems and at low bombarding energies. It is, on the other hand, highly questionable for collisions involving weakly-bound systems. In fact, in this case the initial wavefunction extends so much outwards that a major part of the reaction cross sections does originate at distances where the target gets to be “inside” the transition density.

We have set to investigate in this contribution the role of the nuclear couplings into the continuum excitation spectrum. While the Coulomb field happens to be proportional to a generating function for the Legendre polynomials, no equivalent simplification is available to handle the nuclear field given in eq. (5). But then, once we are forced by the characteristics of the latter to perform numerically the double-integral in eq. (4), there is no compelling reason to continue using the (incorrect) r^λ -response for the Coulomb excitation aspects of the reaction analysis. Actually, by constructing the formfactors for the nuclear and Coulomb components on equal footing one should be able to judge the quality of the approximation introduced in previous treatments. Notice that by keeping the Coulomb integrand explicitly as a function of $\sqrt{r^2 + R^2 - 2rRu}$, an appropriate expansion into either $r^\lambda/R^{\lambda+1}$ or $R^\lambda/r^{\lambda+1}$ is automatically insured even for the point-field given in eq. (6).

It was already stated that the radial wavefunctions $R_{n_1 \ell_1 j_1}(r)$ have been constructed by solving the Schroedinger’s equation for the bound states in a nuclear potential with a Woods-Saxon shape, including Coulomb, centrifugal and spin-orbit components. Similarly, the continuum states $R_{E \ell_2 j_2}(r)$ have been obtained by matching the asymptotic Whittaker’s functions to the numerical solutions constructed within the potentials’ range.

Finally, we briefly recall the reaction formalism in which the formfactors constructed according to these prescriptions are to be applied. We exploit a semiclassical scheme to construct elastic and inelastic cross sections⁹⁾. Asymptotic values of the reaction amplitudes are obtained for each partial wave ℓ as a function of time by solving a set of coupled differential equations of the following form

$$\dot{a}_i^\ell(t) = -i\hbar \sum_{\beta} F_{i\beta}[\vec{R}(t)] \exp[-i(\epsilon_i - \epsilon_j)/\hbar] a_j^\ell(t), \quad (9)$$

where ϵ_i is the intrinsic excitation of the channel i and $\vec{R}(t)$ represents the trajectory of relative motion. This function is integrated as part of the set of time-dependent equations, assuming an ion-ion potential parameterized according to ref.¹¹⁾ ($V_0 = -42.1$ MeV, $R = 9.4$ fm and $a = 0.63$ fm). A first-order elastic phase shift δ_ℓ is also extracted by integrating along the trajectory an optical potential whose imaginary part is assumed to have various plausible forms, as discussed later in the text. Details on the discretization procedure for the continuum states and the explicit expressions used to construct differential and total Q-value distributions can be found in ref.¹⁰⁾.

3. Results for the Reaction ${}^8\text{B} + {}^{208}\text{Pb}$ at 46 MeV/nucleon

We start by providing some insight on the elements that enter in the construction of the formfactors and the origin of the energy-dependence of the strength distributions. We use for this illustration the response associated with the simple r^λ radial field. The reaction that will be considered throughout this section is ${}^8\text{B} + {}^{208}\text{Pb}$ at a high bombarding energy of 46 MeV/nucleon (see ref.⁵⁾). The top of Fig. 1 shows the radial dependence of the continuum wavefunctions $R_{E\ell_2j_2}(r)$ for $\ell_2=0$ and $j_2=1/2$ at three excitation energies, $E=0.3$ MeV (dotted line), $E=0.6$ MeV (solid line) and $E=1.9$ MeV (dashed line). These energies have been chosen to be slightly below, at, and slightly above the energy where the maximum of the response to the chosen field occurs. Note the rapid change of the wavelength near the continuum threshold which makes possible the optimal matching referred to in the Introduction. The lower frame displays the radial integrand $R_{E\ell_2j_2}^*(r)R_{n_1\ell_1j_1}(r)r^3$ for the dipole case, $n_1\ell_1j_1 \equiv (1, 1, 1/2)$, $\ell_2j_2 \equiv (0, 1/2)$ and for the same three values of E . One can here appreciate the unusually large portion of space that is involved in the construction of the couplings between a weakly-bound state and the continuum. For a reference consider the shaded area, where transition densities corresponding to ordinary well-bound states in a system of the size of boron would be entirely localized. Fig. 2 shows the energy distribution of the electromagnetic dipole strength, $dB(E1)/dE$, for the transitions $p_{3/2} \rightarrow s_{1/2}$ and $p_{3/2} \rightarrow d_{5/2}$ (top and bottom frames, respectively). In both cases, the results obtained for the proton excitation (solid lines) are compared

with those obtained for the corresponding neutron excitation, under the assumption of an equal binding energy for the initial $p_{3/2}$ state (dashed lines).

The results collected in Figs. 1,2 are qualitatively similar to the ones reported in ref. 2) for the case of uncharged particles. Note, however, that the calculations in that reference pertained single-neutron transitions in heavy nuclei and were obtained by exploiting analytical expressions valid only for square-well potentials. In addition to the effects of a finite diffuseness, the calculations reported here incorporate the proton confining barrier. This is relevant for the lower part of the energy response. Because of the shorter extent of penetration into the classically forbidden region, the strength distributions for proton transitions are, *ceteris paribus*, peaked at higher excitation energies and acquire a larger width.

Examples of the dipole couplings involved in the single-proton transitions $p_{3/2} \rightarrow s_{1/2}$ and $p_{3/2} \rightarrow d_{5/2}$ are given in Fig. 3 (left and right sides of the figure, respectively). The radial dependence of the formfactors depicted in frames a) and d) are in arbitrary units as the motivation here is only to compare the magnitude of the Coulomb and nuclear terms. This can be done at the level of the double-integrals in eq. (4), where the two components blend at the proper relative scale, thus allowing us to ignore angular-momentum algebra and other common factors. It is seen that for either single-particle transition, the nuclear coupling dominates at center-of-mass distances from 25 fm inwards. This is significant, given the fact that a considerable part of the break-up cross section originates from partial waves that probe distances inside this domain †. The dotted lines correspond to the extrapolation into the shorter distances of the simple $R^{-\lambda-1}$ -dependence. We can see that even for the dipole case, significant deviations from the proper answer start to register inside 20 fm, building up to factors of about two for $R=10$ fm. This is not a small correction for these partial waves, especially if one keeps in mind that cross sections reflect the square of the coupling matrix elements. It may not be overall a major consideration, however, since for $\lambda=1$ a large percentage of the total contribution to Coulomb break-up comes from the large partial waves. Frames b) and e) display another aspect of the formfactors, namely their dependence as a function of the continuum energy at a fixed distance. This has been chosen – for the calculations displayed in the figure – to be 15 fm.

† Note that for energies of the order of 40 MeV/nucleon a classical picture of the relative motion corresponds to one of almost straight-line trajectories and thus the impact parameters and distances of closest approach are almost identical.

Because of the inclusion of the nuclear component and the marked deviations in the Coulomb term an altogether different population pattern for the energy channels above threshold should emerge. This is indeed the case, as it can be seen in the two bottom frames, where the electric response in terms of the square of the matrix elements of the field r^λ is displayed. Notice the significant shift of the maximum of the couplings towards a lower value of the energy. This change would reflect directly in the Q-value distribution of the cross section. In fact, in the adiabatic limit the profiles of both functions coincide.

We have not displayed in Fig. 3 the corresponding information for the transition $p_{3/2} \rightarrow d_{3/2}$. Although the spin-orbit coupling is properly taken into account in our formalism, there are no qualitative aspects in this transition that differ enough from the $d_{5/2}$ case that merit its inclusion here. Insofar as calculating cross sections is concerned, however, dipole transitions $p_{3/2} \rightarrow d_{3/2}$ represent a viable alternative and need to be incorporated in the coupled-channel analysis.

Fig. 4 is analogous in structure to Fig. 3, except that it covers the $\lambda=3$ component of the multipole expansion of the couplings in eq. (4). This is not relevant for the $p_{3/2} \rightarrow s_{1/2}$ transition but is allowed by parity and angular momentum selection rules for the $p_{3/2} \rightarrow d_{3/2}$ and $p_{3/2} \rightarrow d_{5/2}$ transitions into the continuum. It is known that the dependence in multipolarity of the nuclear formfactors is weaker than in the Coulomb case. This is reflected in the figure (referring to the $p_{3/2} \rightarrow d_{5/2}$ transition), where an even more pronounced dominance of the nuclear component is put in evidence. It is interesting to note how much larger are in the octupole case the differences introduced by using the r^λ -response, now associated with a pure R^{-4} radial dependence. Overestimation of the couplings can in this instance involve orders of magnitude. By the same token, calculations of cross sections for Coulomb break-up relying on the $B(E3)$ strength distribution would lead to totally erroneous predictions (compare frames b) and c)). One should stress here that this problem is unrelated to the need of including nuclear processes. That is, the standard procedure to calculate electric dissociation for weakly-bound systems is incorrect even if a justification to leave the nuclear field out of the picture could be found.

We devote the next two figures to indicate how the full range of partial waves contributes to the reaction cross sections and to learn about the effects of an absorptive potential. Fig. 5 shows the relative importance of the different impact parameters, b , in building the cross section for projectile dissociation. For a given channel k the

quantity $d\sigma_k/db$ incorporates three b -dependent factors, namely

$$\frac{d\sigma_k}{db} \propto b |a_k(b)|^2 \exp \left[-2 \int W(R(t)) \Big|_b dt \right] . \quad (10)$$

The modulus squared of the reaction amplitude $a_k(b)$ gives the probability to populate the channel and the exponential introduces, within our model space, the attenuation which takes into account all other degrees of freedom not explicitly included in the formalism (for instance, those related to fusion). This factor is constructed by integrating along the trajectory the imaginary part of the optical potential, $W(R(t))$. For the calculations shown in this figure the absorptive potential has been given the same geometry of the real part and half its strength (i.e. $W_o = -21$ MeV, $R = 9.4$ fm, $a = 0.63$ fm). We focus our attention on a continuum channel at energy $E = 0.6$ MeV and consider for the moment only the dipole transition between the $p_{3/2}$ and $s_{1/2}$ states.

The coupled-channel program has been run three times: with Coulomb couplings only, with nuclear couplings only and with both types of interactions included. The corresponding results for $d\sigma_k/db$ are shown with dotted-, dashed- and solid-lines, respectively. One can see that the nuclear component builds its contribution mostly from impact parameters between 10 and 20 fm. In this range it dominates over the Coulomb part. This one, on the other hand, extends much farther out, as it can be expected from the slow R^{-2} radial dependence of the couplings. The two components – whose formfactors at large distances differ in sign – can interfere in a significant way. Notice, for instance, the dip in $d\sigma_k/db$ at $b \approx 18$ fm where the separate terms have almost identical magnitude, in close correlation with the crossing of the formfactors already shown in Fig. 3. From this figure one can infer that it is safe to ignore nuclear effects for impact parameters larger than $b \approx 30$ fm. This value of b corresponds to an elastic Coulomb scattering angle of about three degrees.

A characteristic ratio of one-half between the imaginary and real parts of the optical potential is often used in the heavy-ion literature in the lack of better judgment. We note, however, that changing this proportion even by factors of two does not affect the qualitative aspects of what has been displayed in Fig. 5. This is due to the fact that the range of the absorption is what mostly determines the effective cut-off for central impact parameters. In a situation involving a projectile with a pronounced proton skin it seems appropriate to test, in addition, the sensitivity of

the results to changes in the absorption range. This question is addressed in Fig. 6, where the radius of the imaginary part of the potential used in the previous figure has been shifted by ± 1 fm. The scope is here slightly different from the one in the previous application, as we plot the function $d\sigma/db$ not for an individual channel but integrated over the entire Q-value range,

$$\frac{d\sigma}{db} \propto b [1 - |a_o|^2] \exp \left[-2 \int W(R(t)) dt \right]. \quad (11)$$

In this expression the first quantity between brackets gives now the global probability to be taken away from the elastic channel. The nuclear component (building up its contribution closer to the central collisions) is naturally more sensitive to the modulation in range than the Coulomb part. The predominant role of the nuclear processes in the 10–25 fm interval of impact parameters is not, however, affected. Note that the scales of the nuclear frames are, for both dipole and octupole transitions, one order of magnitude larger than the corresponding ones for the Coulomb case. It is also interesting to observe that, as a consequence of the combination of many positive-energy channels, the distributions become rather structureless.

Examples of the Q-value dependence of the cross sections for transitions into the continuum are shown in Fig. 7. To the left of the figure we consider the single dipole transition $p_{3/2} \rightarrow s_{1/2}$ and present the separate Coulomb and nuclear components together with the result of their combined action. The interfering character of the two mechanisms is here quite evident. Thus, even though the nuclear contribution is *per se* larger than the Coulomb one, the total cross section is only moderately increased with respect to what would have been (wrongly) predicted in terms of Coulomb dissociation only. There is a small shift of the distribution to higher Q-values and the distribution becomes wider as well. The right-hand-side of the picture displays the total cross section obtained for the transitions $p_{3/2} \rightarrow s_{1/2}$, $p_{3/2} \rightarrow d_{3/2}$ and $p_{3/2} \rightarrow d_{5/2}$ including the dipole and octupole terms, i.e. all the multipolarities allowed by parity and angular momentum selection rules. Notice that the addition of the octupole component increases the tendency to populate channels with higher excitation energy.

In connection with Figs. 3,4 attention was brought to the strong deviations from the true Coulomb formfactors that could be introduced by an indiscriminate reliance on the r^λ -response. We show in Fig. 8 two concrete examples of the actual

manifestation of this effect in reaction cross sections. As an illustration we have here calculated Q -value distributions for the specific transition $p_{3/2} \rightarrow d_{5/2}$; the continuum d -channels are accessible via both dipole and octupole couplings and thus provide a good case to explore the dependence with multipolarity. The solid lines correspond to calculations performed with the microscopically-constructed Coulomb formfactors while the dashed curves have been obtained by replacing them by others with the simple $R^{-\lambda-1}$ radial dependence. While results for the dipole case are not affected in a major way by the substitution – and then only for the lower excitation energies – an improper handling of the octupole couplings would lead to radically different answers. The cross sections are grossly overestimated (as it had been anticipated) but even the profile of the excitation spectrum is altered.

We close this section devoted to the ${}^8\text{B} + {}^{208}\text{Pb}$ reaction at high bombarding energies with Fig. 9. We show here a break-down into components of the Q -value distribution for all the inelastic transitions starting from the bound-, $p_{3/2}$, state in ${}^8\text{B}$ that involve the s and d states in the continuum. The total result is given by the thick solid line and displays a maximum at energies just below the one-MeV level (see also Fig. 7). The other curves show the same quantity, but now only some specific channels and/or multiplicities were included in the calculations. Setting aside the continuum j -quantum number (whose values are left implicit) we identify the different situations as follows: dipole $p \rightarrow s$ transitions (dashed line), dipole $p \rightarrow d$ transitions (dotted line), octupole $p \rightarrow d$ transitions (dash-dotted line) and dipole-plus-octupole $p \rightarrow d$ transitions (thin solid line). It can now be inferred that the fact that the distribution peaks at a low energy is due to a relative predominance of the dipole $p \rightarrow s$ transition in that part of the spectrum. Note, however, that due to the coupled-channel character of the calculation the additivity of these partial results is not entirely justified. Although the order of magnitude of the cross section seems to be correct, at this level the profile of the Q -value distribution deviates from the scarce available evidence. Of course any attempt to compare with data should not ignore electric and magnetic transitions of other multiplicities, which have been discussed in refs. 7).

4. Low-energy Case

We have already emphasized how the long-range of the nuclear formfactors for inelastic excitation of weakly-bound single-particle states leads to features which

are markedly different from those encountered in the excitation of stable systems. We turn in this section to a class of reactions that are normally considered to be totally dominated by electromagnetic processes, namely collisions at bombarding energies below the Coulomb barrier. Within a classical picture one argues that at these energies the trajectories of relative motion cannot explore the internal region where nuclear forces are effective and that, consequently, excitation processes via the nuclear field should be negligible. The possibility of having a “clean” Coulomb dissociation process was, in fact, one of the main motivations for the experiment presented in ref. ⁵⁾, a study of the break-up of ^8B on a ^{58}Ni target at a subbarrier bombarding energy of $E=25.3$ MeV. At this energy, even for the most penetrating, head-on, collisions the distance of closest approach is of the order of 10 fm. This is several nuclear diffuseness outside of the sum of the radii of the reactants and therefore regarded as “safely” outside of the nuclear range of action.

In order to check this point, we have performed calculations of inelastic excitation to the continuum for the $^8\text{B} + ^{58}\text{Ni}$ reaction at the same bombarding energy of the experiment in ref. ⁵⁾. Among the contributing processes with different multipolarity we have specifically considered the transition in which the $p_{3/2}$ proton in ^8B is promoted, via dipole excitation, to a $s_{1/2}$ -state in the continuum. The angular distribution for the global inelastic process – i.e. integrated over all possible excitation energies – is given in Fig. 10. We again compare the full calculation (resulting from the total proton-target interaction) with those that only include either the Coulomb or nuclear couplings. As in a standard situation, the distribution at forward-angles is dominated by the Coulomb excitation mechanism. Nuclear processes, on the other hand, prevail at more backward angles, with a characteristic grazing peak followed by a decrease of the cross sections due to absorption. Note, however, that the peak in the angular distribution (at $\theta \approx 80^\circ$) is associated with a classical trajectory whose distance of closest approach is 12 fm, i.e. considerably larger than the expected range of nuclear forces. Even the trajectory leading to the final angle $\theta=40^\circ$, for which Coulomb and nuclear processes contribute just about equally, has a distance of closest approach of about 20 fm!

The relative importance of the Coulomb and nuclear contributions (which changes with the scattering angle) should also show up in different Q -value profiles. As an example, we display in Fig. 11 the double differential cross section as a function of the excitation energy at fixed values of the scattering angle. The three curves in each frame refer to the full calculation (resulting from the total interaction) and to

calculations that only include either the Coulomb or nuclear couplings. As expected, the forward-angle region (top frame) is dominated by Coulomb dissociation and the shape of the Q -distribution approaches that of the $B(E1)$ distribution (cf. Fig. 3c). This correspondence becomes even closer for smaller angles, as the relevant trajectories probe the formfactors in more external regions. The situation is different for the large angles, where the nuclear contribution is dominant (bottom frame). The Q -value distribution is now peaked at a rather higher energy, reflecting the energy dependence of the formfactors at smaller radii (cf. Fig. 3b). Destructive interference between the nuclear and Coulomb contributions leads to a practically vanishing cross section at an intermediate angle, $\theta=40^\circ$ (middle frame).

5. Closing Remarks

We aimed in this paper to study the role of Coulomb and nuclear processes in the dissociation of ^8B . We have deliberately refrained from developing a new reaction formalism and chosen instead to approach the problem with well-known tools introduced for the treatment of inelastic processes in heavy ion reactions. These call for the formfactors to be constructed from a folding of the relevant transition densities with the Coulomb and nuclear excitation fields. The procedure, by construction, treats both components on equal footing and immediately provides ways to compare the relative importance of the coupling strengths.

From this point of view it is quite clear that if a given mechanism manages to stretch the transition densities out – as it is the case when weakly-bound orbitals come into play – the situation is likely to affect the nuclear component much more than the Coulomb one. In fact, the Coulomb coupling, being naturally long-ranged, cannot benefit from this novel feature as much as its nuclear counterpart. The latter, as it is well-known, does rely on the close contact between densities and excitation fields.

The conclusions we have reached concerning the primary role of the nuclear processes in the proton dissociation of ^8B are significantly at odds with the standard interpretation of this phenomenon. Clearly it does not make sense to extract from the available data any conclusion on interfering E1, M1 and E2 processes if the electromagnetic couplings do not play a dominant role. In this perspective reported

fittings to data, when only based on Coulomb dissociation, may have to be dismissed altogether. Actually, a critical inspection of Coulomb dissociation studies could have provided some warning about their weakness, since the range of relevant impact parameters was often loosely specified or merely chosen to reproduce the observed cross sections. We have let, on the other hand, ordinary nuclear dynamics dictate on this question and the answers – even allowing for rather different absorption geometries – consistently reveal a substantial range of partial waves where the nuclear couplings dominate.

One could argue that our formalism, developed and successfully tested for heavier ions, may need some adjustment if transported to the realm of light, weakly-bound nuclear systems. Still, the magnitudes presently at play so significantly tilt the balance of the reaction in the direction of the nuclear component that the resulting patterns should survive even more than just a fine tuning of the reaction mechanism.

To shed additional light on these fundamental questions consideration should perhaps be given to an alternative formulation. We refer to that of treating the dissociation of the projectile in terms of the transfer of the proton to the target in either bound or continuum states. A good understanding of this complementary view could help revealing eventual shortcomings in the approach that we have followed to reach our conclusions. We understand that investigations along this track are being pursued¹²⁾.

This work was partially supported by the Danish Natural Science Research Council, the Danish Ministry of Education and by the INFN.

References

1. H. Sagawa, N. Van Giai, N. Takigawa, M. Ishihara and K. Yazaki, in Proc. Riken Int. Workshop 1993; H. Sagawa, N. Van Giai, N. Takigawa, M. Ishihara and K. Yazaki, Z. Phys. **A351** (1995) 385
2. F. Catara, C.H. Dasso and A. Vitturi, Nucl. Phys. **A602** (1996) 181
3. I. Hamamoto, H. Sagawa and X.Z. Zhang, Phys. Rev. **C53** (1996) 765; I. Hamamoto and H. Sagawa, Phys. Rev. **C53** (1996) R1492; I. Hamamoto and H. Sagawa, Phys. Rev. **C54** (1996) 2369; I. Hamamoto and H. Sagawa, Phys. Lett. **B394** (1997) 1; I. Hamamoto, H. Sagawa and X.Z. Zhang, Phys. Rev. **C55** (1997) 2361; F. Ghielmetti, G. Colò, E. Vigezzi, P.F. Bortignon and R.A. Broglia, Phys. Rev. **C54** (1996) 2134R
4. T. Motobayashi *et al*, Phys. Rev. Lett. **73** (1994) 2680; T. Kikuchi *et al*, Phys. Lett. **391B** (1997) 261
5. J.J. Kolata *et al*, Nucl. Phys. **A616** (1997) 137c
6. R.A. Broglia, C.H. Dasso, G. Pollarolo and A. Winther, Phys. Rep. **48C** (1978) 351.
7. H. Esbensen and G.F. Bertsch, Nucl Phys. **A600** (1996) 37; C.A. Bertulani, Nucl. Phys. **A587** (1995) 318; Zeit. Phys. **A396** (1996) 293
8. G.F. Bertsch and H. Esbensen, Ann. Phys. **209** (1991) 327
9. K. Alder and A. Winther, *Electromagnetic excitations* (North Holland, Amsterdam, 1975); R.A. Broglia and A. Winther, *Heavy ion reactions* (Addison-Wesley, Redwood City, 1991)
10. C.H. Dasso, S.M. Lenzi and A. Vitturi, Nucl. Phys. **A611** (1996) 124
11. O. Akyuz and A. Winther, in *Proceedings of the Enrico Fermi International School of Physics, 1979, Course on Nuclear Structure and Heavy Ion Reactions*, Ed. R.A. Broglia, C.H. Dasso and R.A. Ricci (North Holland, Amsterdam, 1991)
12. A. Bonaccorso, Phys. Rev. **C53** (1996) 849; A. Bonaccorso and N. Vinh Mau, Nucl. Phys. **A615** (1997) 245
13. A. Bohr and B. Mottelson, in *Nuclear Structure Vol. I*, W.A. Benjamin, Reading, 1969

Figure captions

Fig. 1 – a) radial dependence of the $\ell=0$ proton wavefunction in the continuum at three different energies. These have been chosen to be at the maximum of the $B(E1)$ strength distribution ($E=0.6$ MeV, solid line) and two other values, above ($E=1.9$ MeV, dashed line) and below ($E=0.3$ MeV, dotted line) this one. The shaded area indicates the extent of the binding potential in the ${}^8\text{B}$ nucleus. b) Radial dependence of the integrand which yields the values of the $B(E1)$ r^λ -response for the three energies quoted above. The identification of the curves corresponds also to the one for the upper frame. The wavefunction for the initial, bound configuration, has been chosen as a $\ell=1$ proton wavefunction with a binding energy of 140 KeV.

Fig. 2 – Differential distribution of the electromagnetic dipole strength, $dB(E1)/dE$, for the transitions $p_{3/2} \rightarrow s_{1/2}$ and $p_{3/2} \rightarrow d_{5/2}$ (top and bottom frames, respectively). In both cases, the results obtained for the proton excitation (solid lines) are compared with those obtained for the corresponding neutron excitation (dashed lines). The proton and neutron potentials have been adjusted in order to give the same binding energy (0.14 MeV) to the initial $p_{3/2}$ state.

Fig. 3 – Dipole formfactors for the single proton transitions $p_{3/2} \rightarrow s_{1/2}$ and $p_{3/2} \rightarrow d_{5/2}$ (left and right sides of the figure). The reaction is ${}^8\text{B} + {}^{208}\text{Pb}$ at a bombarding energy of 372 MeV. In the top frames Coulomb and nuclear formfactors (solid and dashed lines, respectively) are shown as a function of the ion-ion distance R for an excitation energy in the continuum that corresponds to the maximum of the corresponding electric $B(E1)$ distribution (shown in the bottom frames). Also shown as dotted lines the extrapolation into shorter distances of the simple $R^{-\lambda-1}$ dependence. In the middle frames the Coulomb and nuclear formfactors are shown as a function of the excitation energy for fixed distance ($R = 15 fm$). For the absolute scales, cf. text.

Fig. 4 – Analogous to Fig. 3, but for the transition $p_{3/2} \rightarrow d_{5/2}$ and angular momentum transfer of $\lambda = 3$. Labeling of the curves follows the same convention as in the caption to the previous figure.

Fig. 5 Localization of the reaction cross section as a function of the impact parameter. The reaction is ${}^8\text{B} + {}^{208}\text{Pb}$ at a bombarding energy of 372 MeV. The calculations are for the single dipole transition $p_{3/2} \rightarrow s_{1/2}$ and correspond to a channel at excitation energy $E=0.6$ MeV. Three separate runs of the coupled-channel program have produced the curves. They were done including Coulomb couplings only (dotted line), nuclear couplings only (dashed line) and both types of interactions (full line).

Fig. 6 Localization of the reaction cross section as a function of the impact parameter and its dependence as a function of the range of the absorptive potential. The reaction is ${}^8\text{B} + {}^{208}\text{Pb}$ at a bombarding energy of 372 MeV. The cross sections depicted here are summed over all the continuum channels included for the transitions $p_{3/2} \rightarrow s_{1/2}$, $p_{3/2} \rightarrow d_{3/2}$ and $p_{3/2} \rightarrow d_{5/2}$. The left column shows the dipole contribution to the multipole expansion and the right one the octupole term. The full line results from using an imaginary potential with the same geometry as the real part and half its strength. To obtain the dashed and dotted curves the radius of the absorptive potential has been changed by adding and subtracting 1 fm, respectively.

Fig. 7 Q-value dependence of the inelastic cross sections into the continuum. The reaction is ${}^8\text{B} + {}^{208}\text{Pb}$ at a bombarding energy of 372 MeV. The curves depicted here emerge from separate calculations where the reaction amplitudes have been constructed including Coulomb couplings only (dotted line), nuclear couplings only (dashed line) and both types of interactions (full line). The left frame corresponds to the dipole transitions $p_{3/2} \rightarrow s_{1/2}$. To the right, the information applies to the total cross section accumulated from the dipole and octupole terms and thus exhaust the possibilities afforded by $p \rightarrow s$ and $p \rightarrow d$ transitions.

Fig. 8 Comparison between cross sections for electric dissociation constructed with the microscopically calculated Coulomb formfactors and those with the simple $R^{-\lambda-1}$ radial dependence. The frame to the left shows the difference in the predictions for the dipole case, while the right frame corresponds to the octupole case.

Fig. 9 Break-down of the Q-value distribution for all inelastic transitions from the bound-, $p_{3/2}$, state in ${}^8\text{B}$ to $s_{1/2}$ and $d_{3/2,5/2}$ states in the continuum.

The thick solid line contains the combined effect of the dipole and octupole couplings and thus coincides with the one already displayed in Fig. 7. The other curves indicate the corresponding quantity but for different truncations of this set of reactions channels. These are: $p_{3/2} \rightarrow s_{1/2}$, $\lambda=1$ (dashed line), $p_{3/2} \rightarrow d_{3/2}$ and $p_{3/2} \rightarrow d_{5/2}$, $\lambda=1$ (dotted line) $p_{3/2} \rightarrow d_{3/2}$ and $p_{3/2} \rightarrow d_{5/2}$, $\lambda=3$ (dash-dotted line) $p_{3/2} \rightarrow d_{3/2}$ and $p_{3/2} \rightarrow d_{5/2}$, $\lambda=1,3$ (thin solid line).

Fig. 10 Calculated angular distribution for the reaction ${}^8\text{B} + {}^{58}\text{Ni}$ at bombarding energy $E = 25.3$ MeV, for the dipole transition $p_{3/2} \rightarrow s_{1/2}$, summed over the final energy distribution. The dotted line is the prediction when only Coulomb excitation is included, the dashed line the corresponding nuclear contribution. The solid line gives the predicted angular distribution including both processes.

Fig. 11 Double differential cross section for the reaction ${}^8\text{B} + {}^{58}\text{Ni}$ at $E=25.3$ MeV as a function of the excitation energy, at fixed values of the scattering angle (in the c.m. system). For each angle the curves refer to Coulomb excitation (dotted), nuclear excitation (dashed) and total (solid).

${}^8\text{B}$ (proton)

$p_{3/2} - s_{1/2}(c)$

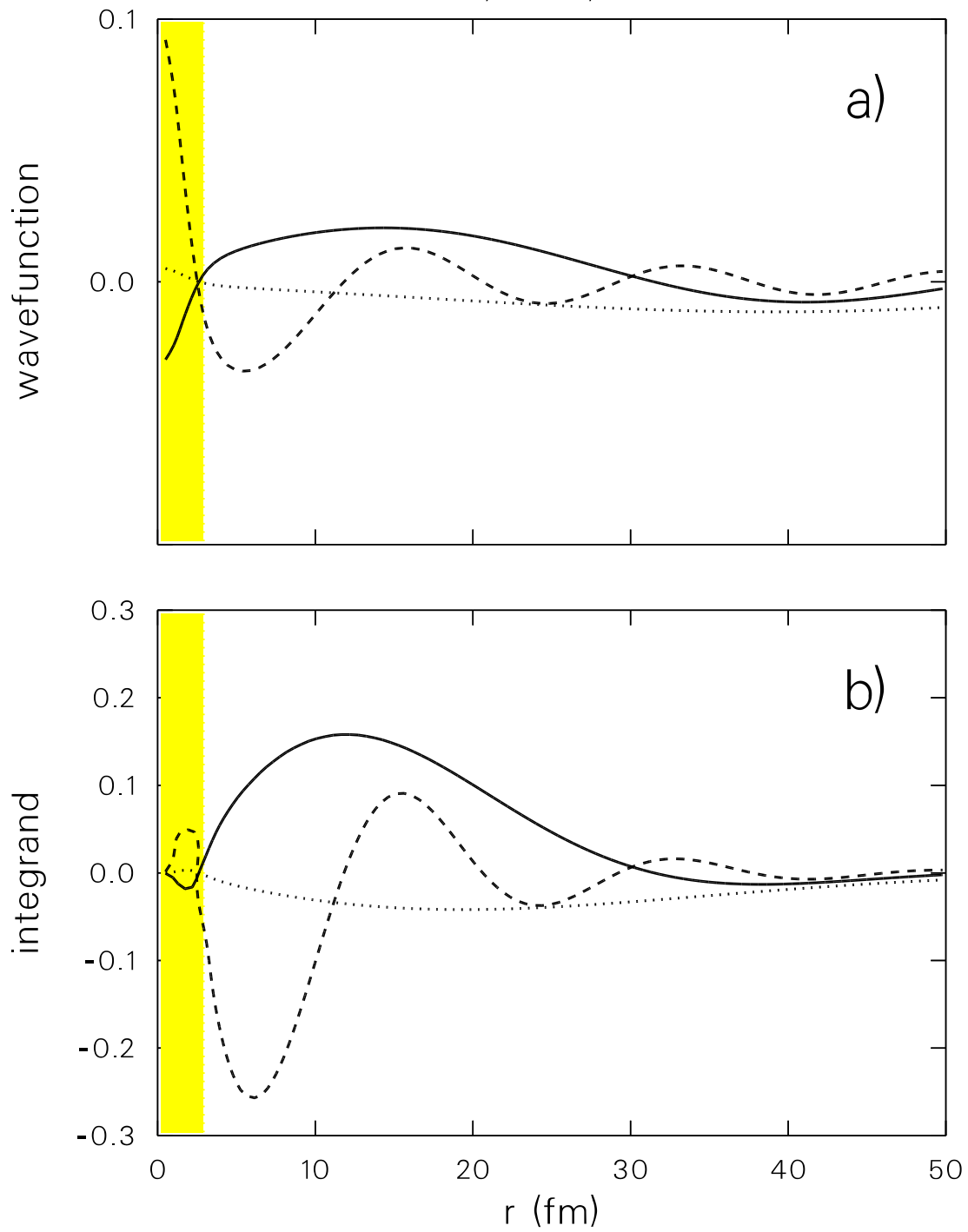


Fig. 1

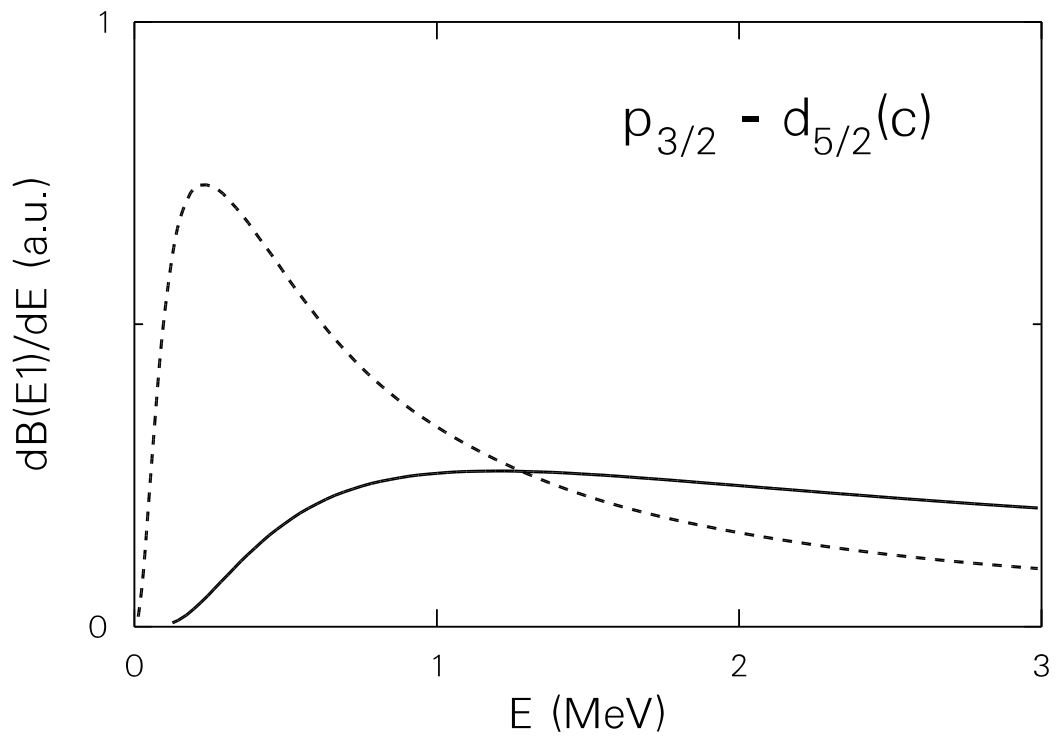
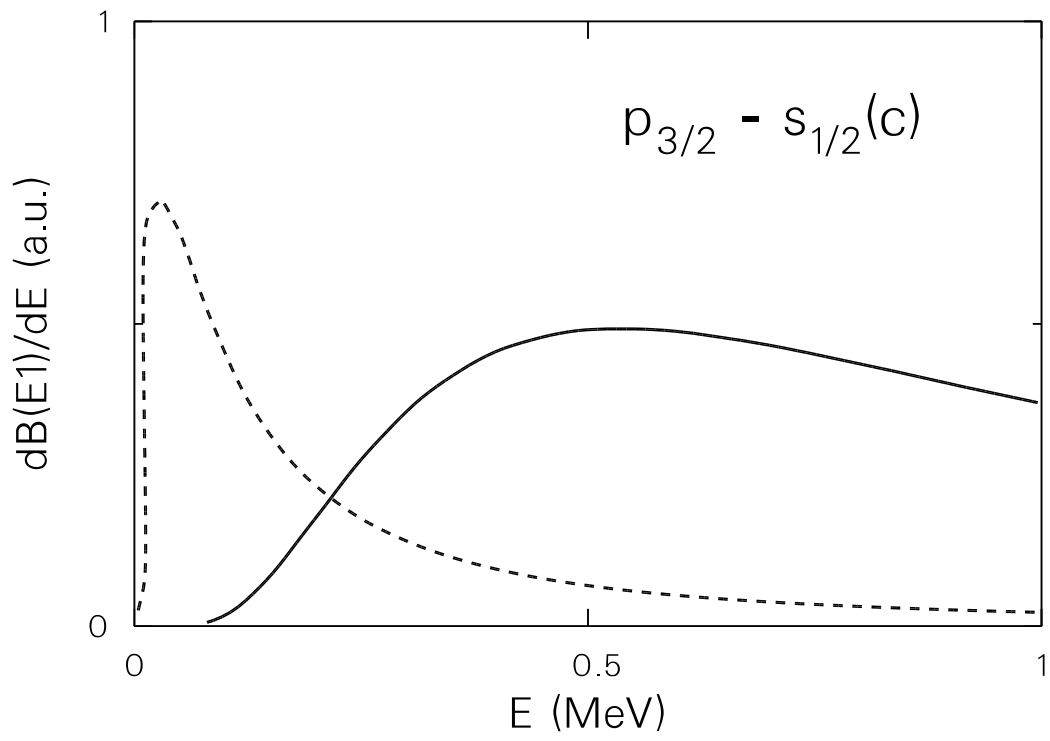


Fig. 2

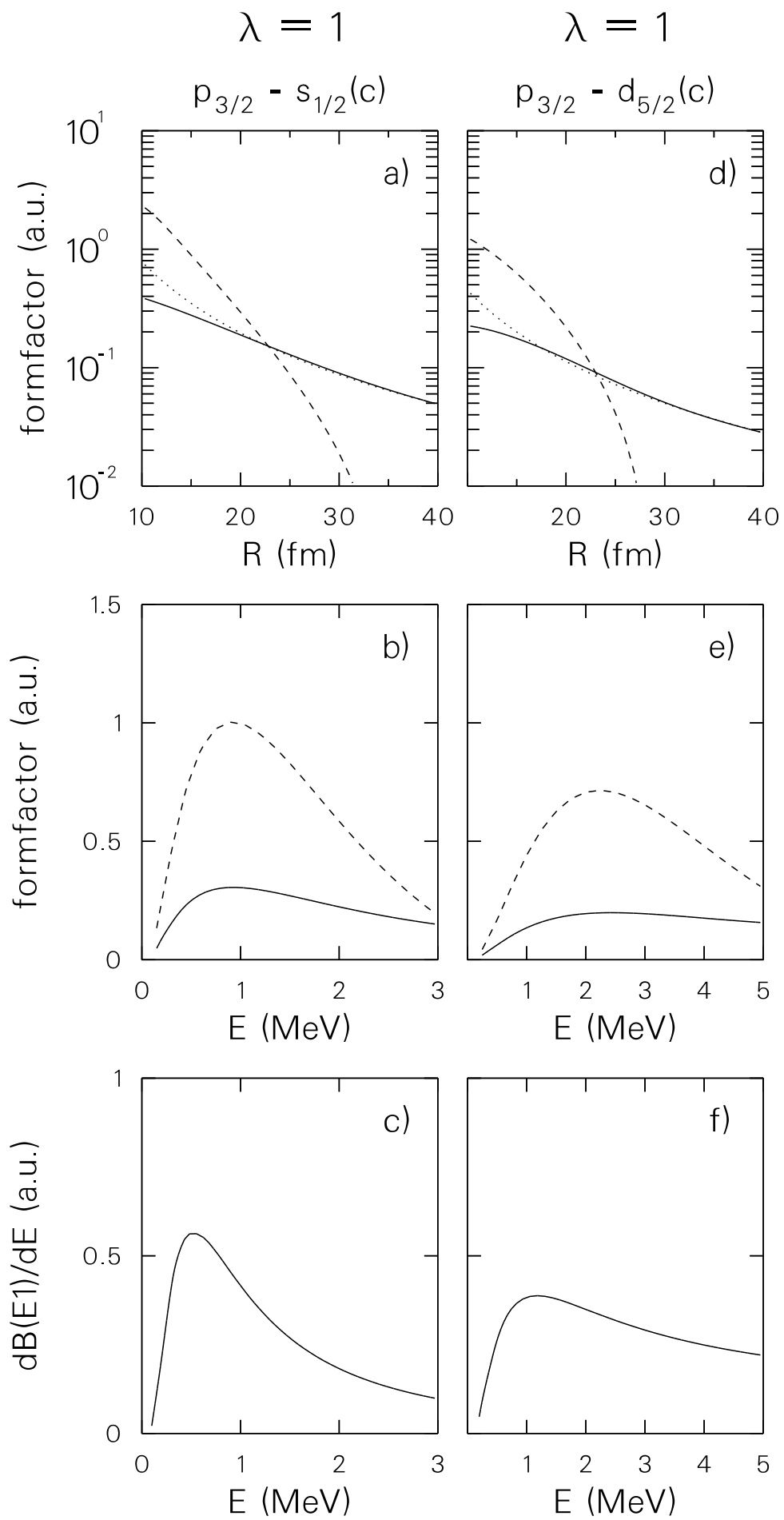


Fig. 3

$$\lambda = 3$$

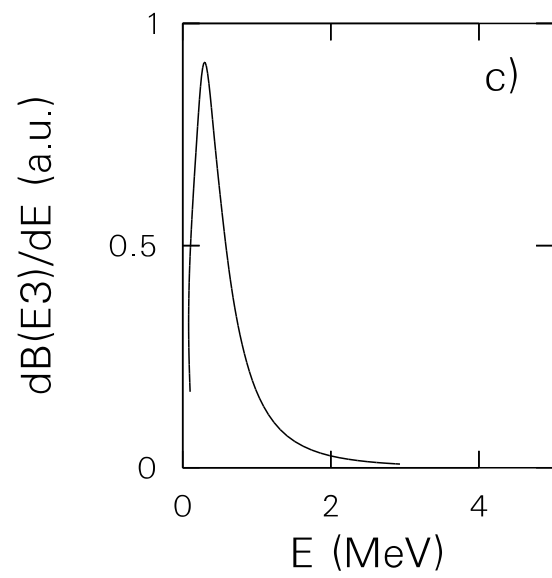
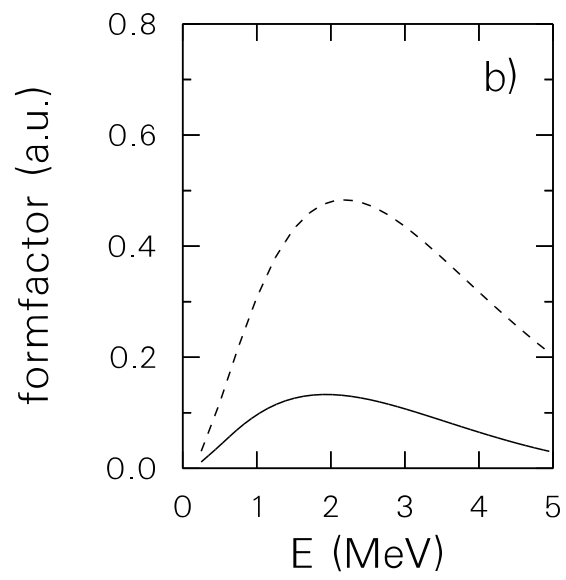
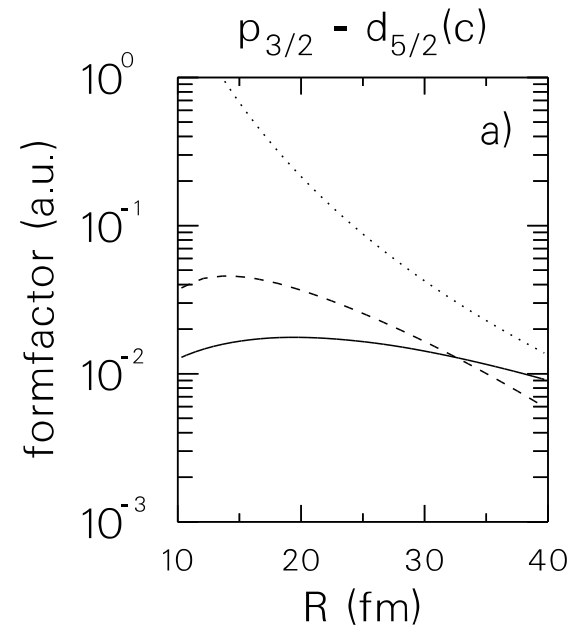


Fig. 4

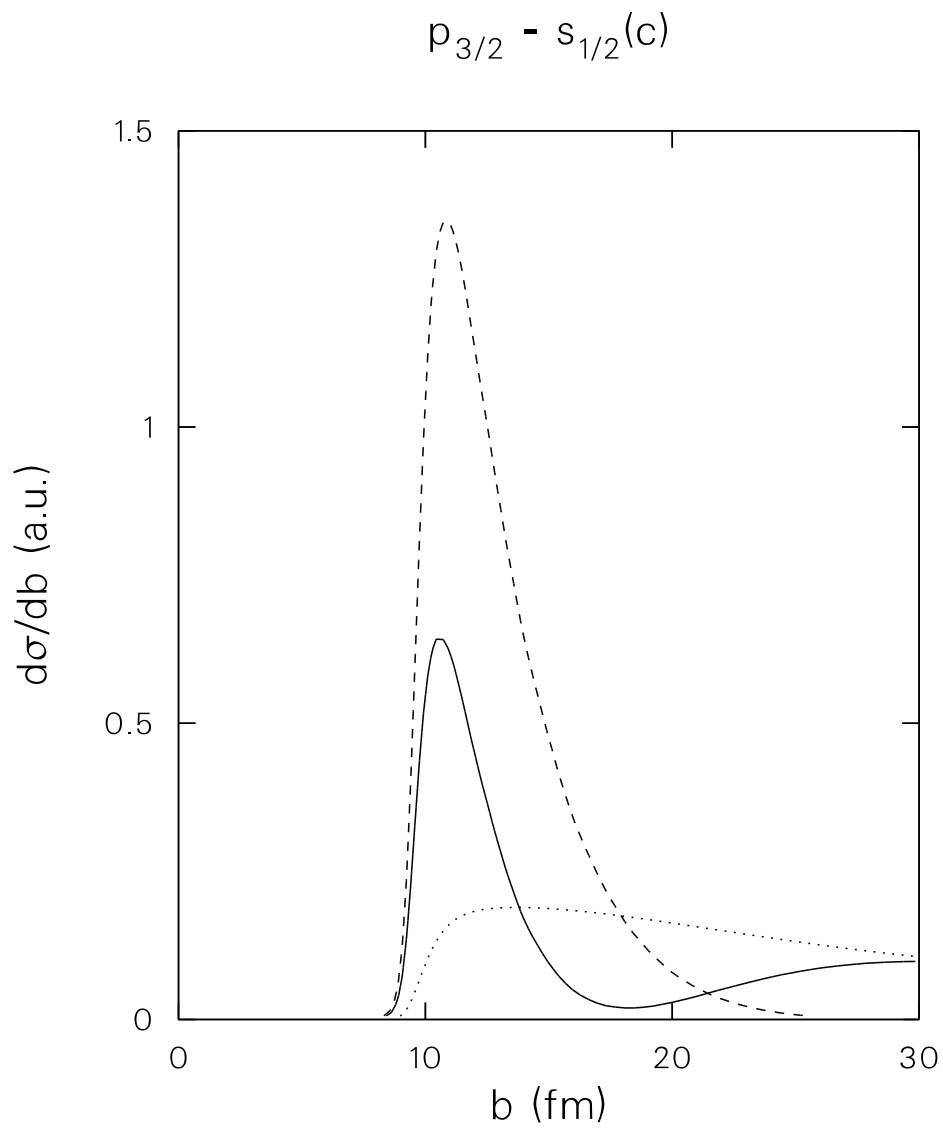


Fig. 5

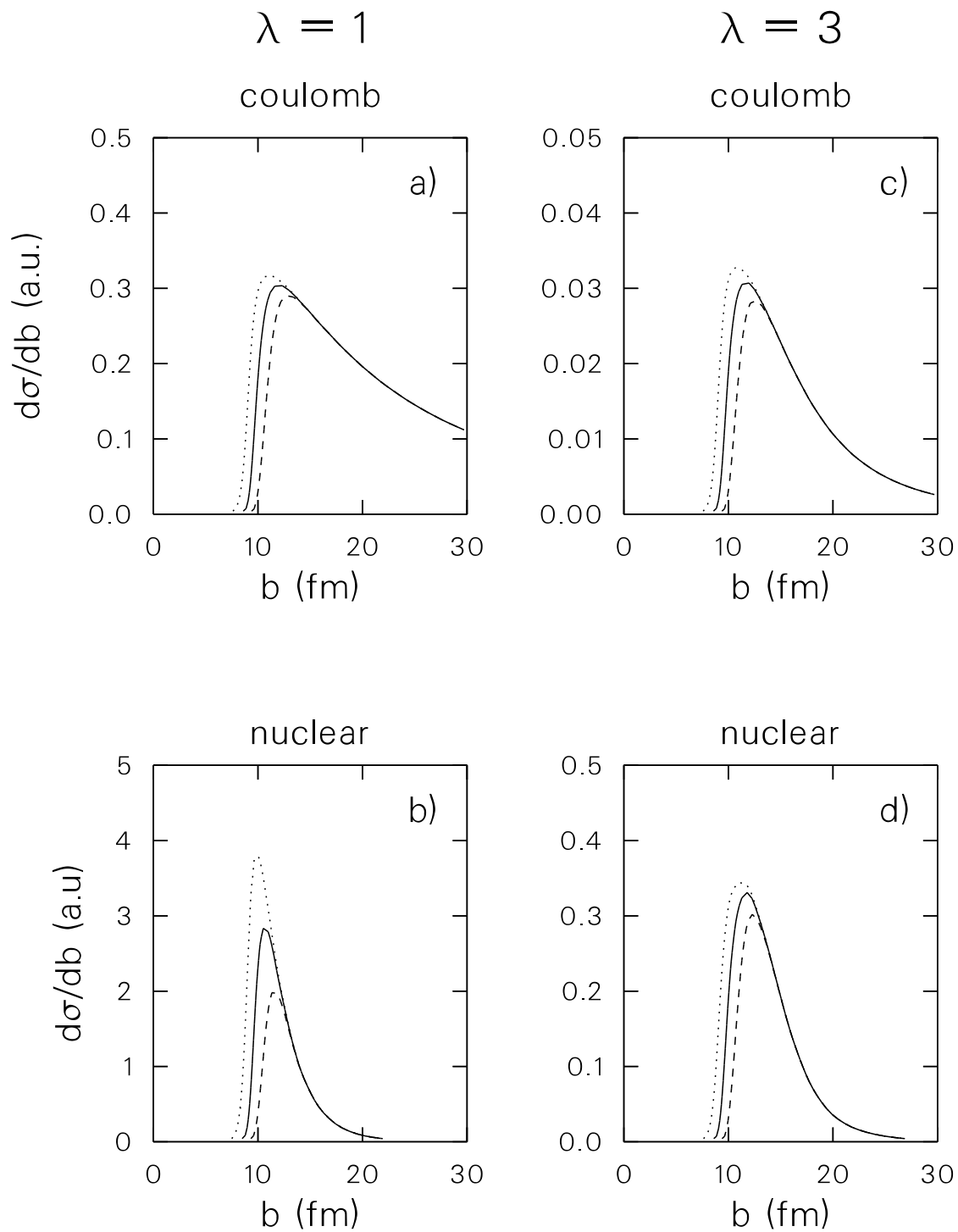


Fig. 6

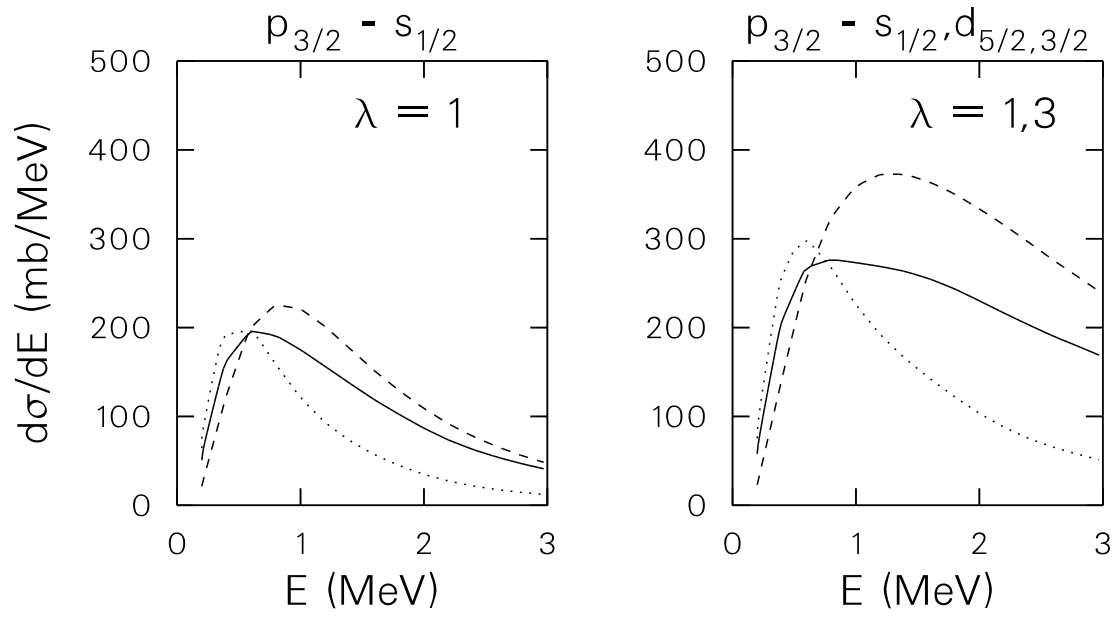


Fig. 7

$$p_{3/2} - d_{5/2}(c)$$

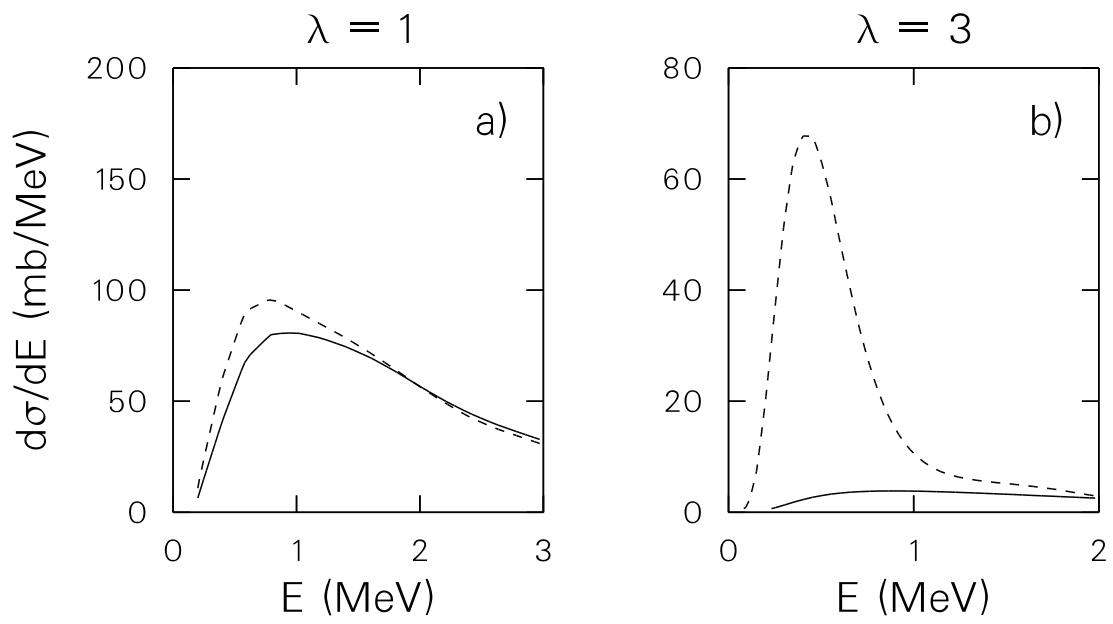


Fig. 8

${}^8\text{B} + {}^{208}\text{Pb}$ (372 MeV)

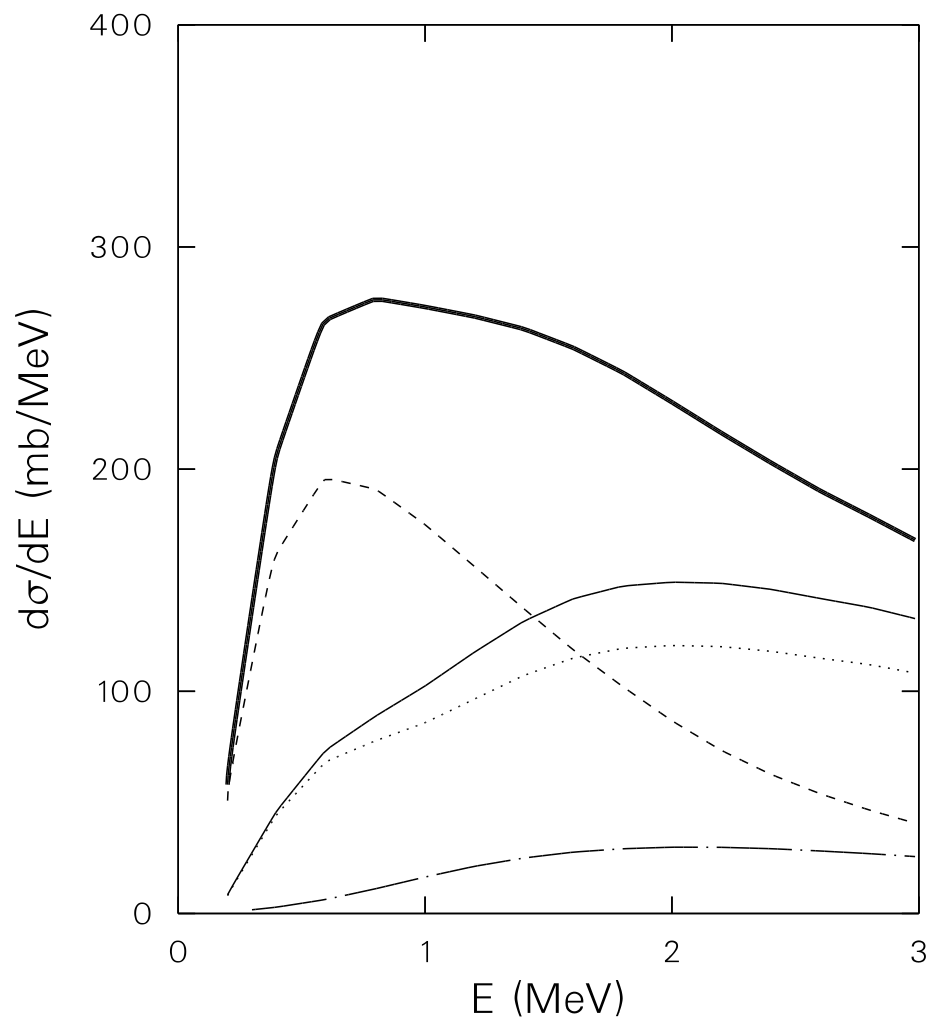


Fig. 9

${}^8\text{B} + {}^{58}\text{Ni}$ ($E = 25.3$ MeV)

$p_{3/2} - s_{1/2}(c)$

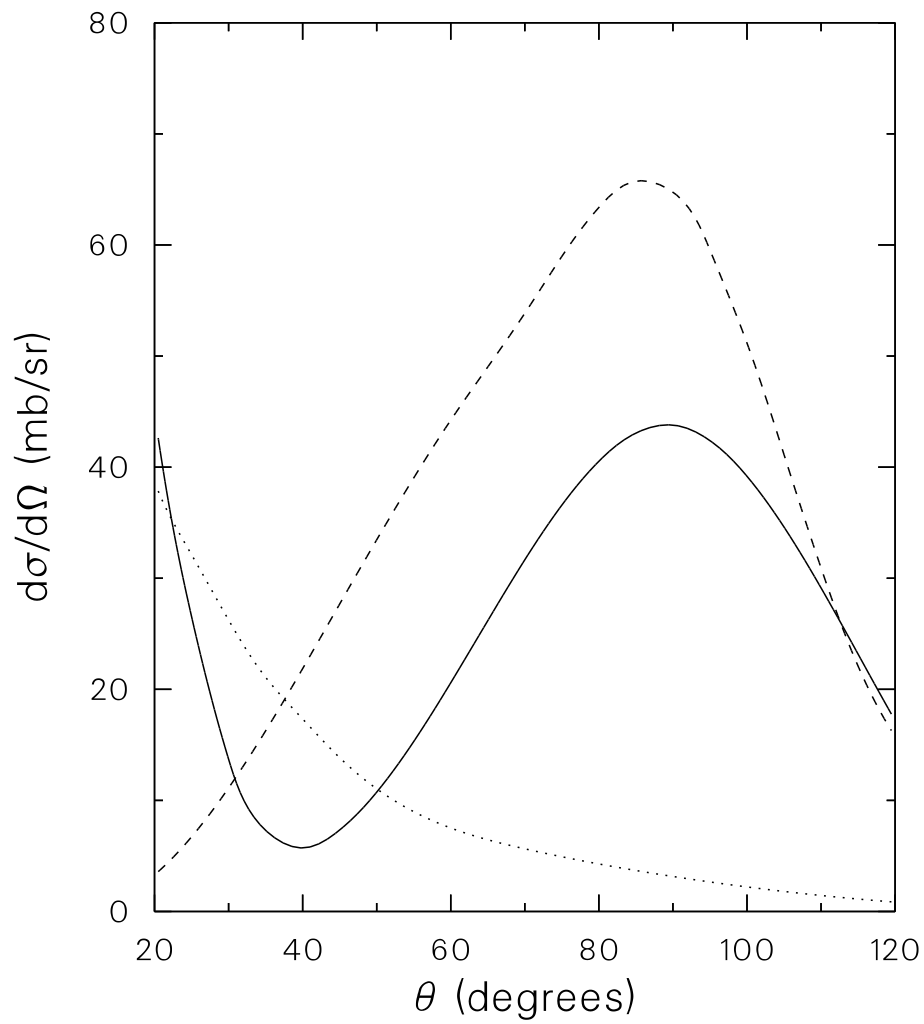


Fig. 10

$^8\text{B} + ^{58}\text{Ni}$ ($E = 25.3$ MeV)

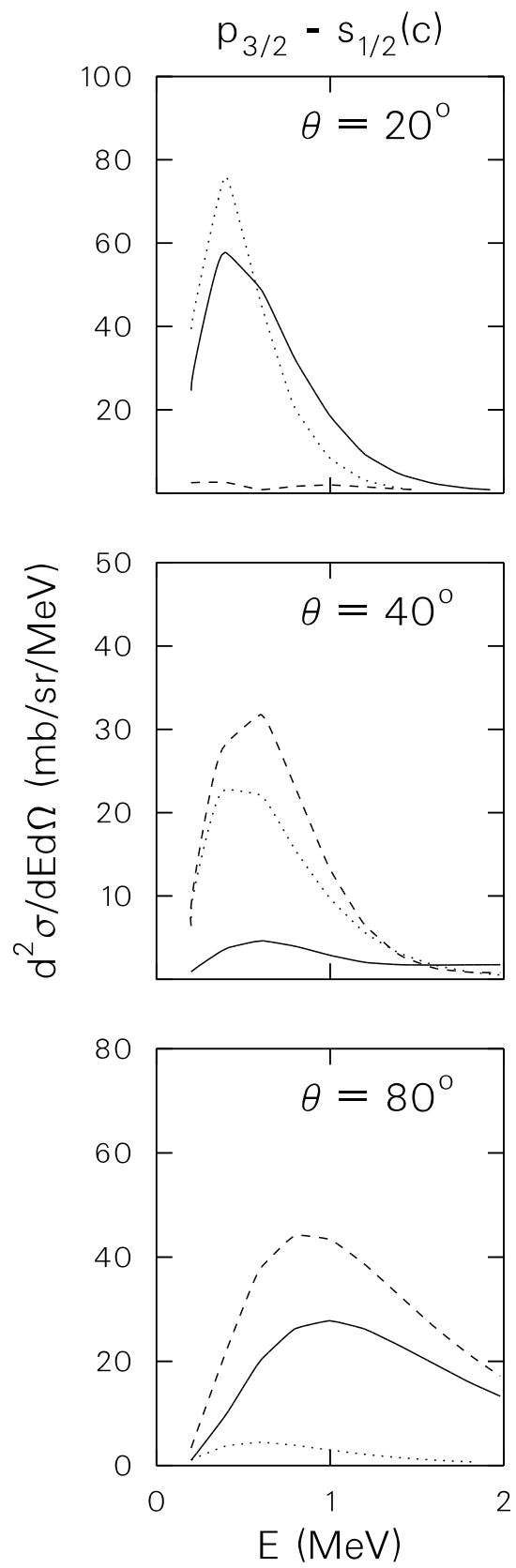


Fig. 11